*reactions*

MDPI

*Article*

# An Iron(III) Complex with Pincer Ligand—Catalytic Water Oxidation through Controllable Ligand Exchange

**Sahir M. Al-Zuraiji [1,2], Dávid Lukács [1], Miklós Németh [1], Krisztina Frey [1], Tímea Benkó [1], Levente Illés [3] and József S. Pap [1,*]**

1 Surface Chemistry and Catalysis Department, Centre for Energy Research, H-1121, Konkoly-Thege Street 29-33, 1525 Budapest, Hungary; sahir.aziz@energia.mta.hu (S.M.A.-Z.); lukacs.david@energia.mta.hu (D.L.); nemeth.miklos@energia.mta.hu (M.N.); frey.krisztina@energia.mta.hu (K.F.); benko.timea@energia.mta.hu (T.B.)

2 Doctoral School on Materials Sciences and Technologies, Óbuda University, H-1034 Bécsi Street 96/b, 1034 Budapest, Hungary

3 Institute of Technical Physics and Materials Science, Centre for Energy Research, H-1121, Konkoly-Thege Street 29-33, 1525 Budapest, Hungary; illes.levente@energia.mta.hu

* Correspondence: pap.jozsef@energia.mta.hu; Tel.: +36-1-392-3284

Received: 21 July 2020; Accepted: 10 August 2020; Published: 13 August 2020


**Abstract:** Pincer ligands occupy three coplanar sites at metal centers and often support both stability and reactivity. The five-coordinate [$Fe^{III}Cl_2$(tia-BAI)] complex (tia-$BAI^-$ = 1,3-bis(2′-thiazolylimino)isoindolinate(−)) was considered as a potential pre-catalyst for water oxidation providing the active form *via* the exchange of chloride ligands to water molecules. The tia-$BAI^-$ pincer ligand renders water-insolubility to the Fe–(tia-BAI) assembly, but it tolerates the presence of water in acetone and produces electrocatalytic current in cyclic voltammetry associated with molecular water oxidation catalysis. Upon addition of water to [$Fe^{III}Cl_2$(tia-BAI)] in acetone the changes in the $Fe^{3+/2+}$ redox transition and the UV-visible spectra could be associated with solvent-dependent equilibria between the aqua and chloride complex forms. Immobilization of the complex from methanol on indium-tin-oxide (ITO) electrode by means of drop-casting resulted in water oxidation catalysis in borate buffer. The $O_2$ detected by gas chromatography upon electrolysis at pH 8.3 indicates >80% Faraday efficiency by a TON > 193. The investigation of the complex/ITO assembly by scanning electron microscopy (SEM), energy dispersive X-ray spectroscopy (EDX), X-ray photoelectron spectroscopy (XPS) before and after electrolysis, and re-dissolution tests suggest that an immobilized molecular catalyst is responsible for catalysis and de-activation occurs by depletion of the metal.

**Keywords:** iron complex; water oxidation; molecular precursor; pincer ligand; immobilization

## 1. Introduction

Artificial photosynthesis, on the analogy of the natural process, is an exciting strategy that may meaningfully contribute to our sustainable-energy future. However, the water oxidation reaction (Equation (1)) still stands as a great challenge in artificial systems, not only because it is an energetically uphill process, but also due to its kinetics making catalysis indispensable [1], as happens at the $Mn_4CaO_5$ active site of the oxygen-evolving enzyme of photosystem II [2].

$$2H_2O \rightarrow O_2 + 4H^+ + 4e^- \quad E^\circ = +1.23\ V - \frac{2.303RT}{F}pH \tag{1}$$

Molecular water oxidation catalysts (WOCs) promote this field by providing mechanistic insight into the complex process of the O=O bond formation. A number of Ru- and Ir-based WOCs have been reported to combine efficiency with robustness and these noble metal complexes have given impetus to this research field [3,4]. Recently, various homogeneous catalysts and electrocatalysts based on earth-abundant metals such as manganese [5–7], iron [8–11], cobalt [12–14], nickel [15,16], and copper [17,18] were paid considerable attention. Progress with molecular catalysts based on abundant, nonprecious and nontoxic transition metals is especially fascinating [19] because economical and large-scale applications in the future are better based on environmentally friendly and available raw materials [20]. In addition, molecular catalysts can be modified by standard chemical synthesis and incorporated into molecular or hybrid molecular-material assemblies for energy conversion [8], although robustness is still an issue that hinders their immediate practical application.

Iron is a prominent candidate for developing cost-efficient WOCs. High-valent iron-oxygen species are very powerful oxidants, which are responsible for substrate oxidation in several enzymes [21–23], organic synthesis and catalytic applications [24,25], including water oxidation. In addition to the selection of the conditions [26], the activity of iron complexes is highly susceptible to electronic and geometric features, too, due to the occurrence of different oxidation and spin states. Therefore finding ligand architectures robust enough to favor the generation and stabilization of high-valent species and WOC remains challenging [26,27].

The first evidence about iron complexes catalyzing the oxidation of water in the early 1980s [28] was followed only by a few other examples until 2010 [10,29]. More recently, different types of homogeneous Fe-based WOCs have been described [20,30–37]. According to the light-driven (LD) [38], chemical (by ceric ammonium nitrate, CAN) [39], or electrochemical (EC) activation mode [8,9,11] of the Fe-WOCs, some typical representatives have been summarized in Figure 1.

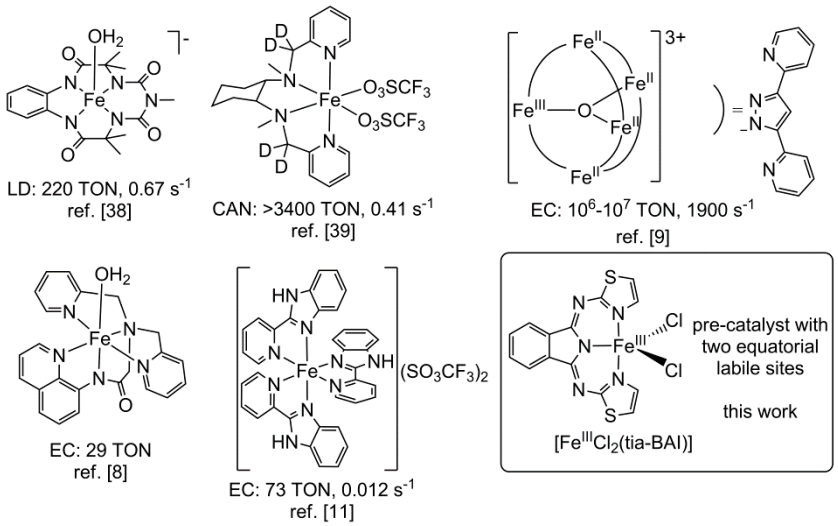


**Figure 1.** Selected representative molecular Fe-WOCs with associated catalytic capabilities, if applicable. WOCS: water oxidation catalysts.

From the known examples for neutral, multidentate aminopyridyl ligands it could be concluded that two labile sites in *cis*-position are preferred by tetradentate ancillary ligands to achieve the best catalytic activity, while complexes with neutral bi-, tri- or pentadentate ligands are inactive [20,32–34,39]. In addition, complexes with tetradentate ligands and *trans*-labile sites show poor or zero activity, except for the Fe complexes that possess rigid polypyridyl ligands, which are a largely different type of compounds [20].

In their comprehensive work Lloret-Fillol and Costas [20,40] also highlight the key role of the *cis*-hydroxide/aqua ligand in the mechanism of the O–O bond formation, that is, binding and orienting the incoming $H_2O$ substrate toward the reactive Fe=O unit. Computations showed that

the proton-coupled electron transfer (PCET) process significantly reduces the energy need to access the high oxidation state reactive intermediate $Fe^{V}(O)(OH)$. However, when PCET is ruled out by the ligand environment (for example, pentadentate amines), single-electron oxidation of $Fe^{IV}(O)$ complexes require much larger, inaccessibly high redox potentials [40]. Note that for the Fe catalysts, the multinuclear structure helps circumventing of the higher oxidation states, mimicking the case of the natural $Mn_4CaO_5$ system of the PS II. The required oxidizing equivalents to trigger WOC in this case are shared between multiple metal sites, thus the iron catalysts can rely on the $Fe^{II}/Fe^{III}$ and $Fe^{III}/Fe^{IV}$ redox transitions. In the key O–O bond formation step the interaction of two proximate M=O intermediates (I2M mechanism) may occur, as it was evidenced for a penta-iron catalyst [9].

Beyond the mechanistic aspects, in practical electrolysis and dye-sensitized photoelectrolysis cells further considerations have to be made. In such cells, instead of dissolved in the electrolyte, catalysts are better applied on conductive surfaces [41,42]. The conversion or degradation of homogeneous Fe catalysts due to the oxidation of ligands [43,44] as well as the question of homogeneous vs. heterogeneous reaction are crucial issues from the viewpoint of the application [26]. Although detailed studies are performed rather often on either homogeneous or heterogeneous systems, the link between the two scenarios is an additional viewpoint in order to produce economically effective WOCs [26,45].

There have been successful attempts to graft the molecular reactivity onto conductive substrates through immobilization, thus providing advanced heterogeneous systems [42]. Shi et al. demonstrated the convenient preparation of nanostructures by applying $Fe^{II}$-phthalocyanine/carbon nitride nanosheet (FePc/CN) nanocomposites [46]. Mono- and binuclear iron corroles were also successfully immobilized in Nafion films and acted as electrochemical WOCs [34]. A tetraazamacrocyclic ligand-based catalyst was also successfully immobilized by mixing with carbon black [47]. Furthermore, we reported the mononuclear $[Fe(PBI)_3](O_3SCF_3)_2$ complex with the nonsymmetric, bidentate ligand 2–(2′–pyridyl)benzimidazole (PBI) [48] as immobilized, self-supported catalyst on oxide semiconductor (Figure 1) [11]. Dissociation of a PBI ligand from the complex in solvent mixtures containing water resulted in two *cis*-labile positions accessible to water molecules thus yielding the catalytically active species. The water-insoluble ancillary ligands aided the immobilization of $[Fe(PBI)_3](OTf)_2$ on indium tin oxide (ITO) electrode, and the solid complex ad-layer was suitable for long-term $O_2$ production immersed in borate buffer at pH 8.3, without noticeable detaching of the active layer.

The above results encouraged us to further investigate water-insoluble Fe complexes as immobilized molecular WOCs with an ancillary ligand type, which was expected to form durable Fe complex and favor its attachment to the surface. Pincer ligands seemed to be promising for this aim with their versatility, wide applications in organic synthesis and catalysis [49]. The 1,3-*bis*(arylimino)isoindolines (BAIs) are 3N donor ligands that have been utilized in iron complexes exerting oxidative reactivity against organic substrates [50,51]. To our knowledge, BAI complexes have never been reported as WOCs. Due to the rigid structure this type of ligand coordinates in a meridional fashion, while the extended $\pi$-delocalization warrants robustness and it is also expected to favor surface immobilization. In addition to the three aromatic nitrogen donor groups, labile sites are accessible for solvent coordination. In this study the ligand 1,3-*bis*(2′-thiazolylimino)isoindoline (tia-BAIH) will be introduced as ancillary ligand in a WOC system. The tia-BAIH forms the characterized $Fe^{III}$ complex, $[Fe^{III}Cl_2(\text{tia-BAI})]$ selectively (Figure 1) [51] that appears as a suitable precatalyst sufficiently soluble in organic solvents, but insoluble in water. We show that the exchange of the chloride to aqua ligands occurs upon the addition of water to the solution of the complex in organic solvents that in turn leads to electrocatalytic water oxidation. It will be discussed that the ancillary ligand allows immobilization of $[Fe^{III}Cl_2(\text{tia-BAI})]$ on indium tin oxide (ITO) electrode, and the ad-layer acts as electrocatalysis in aqueous buffers.

## 2. Materials and Methods

### *2.1. Materials Synthesis*

Solvents (acetonitrile, acetone, methanol, and ethanol, HPLC grade), $D_2O$ (99.8%), tetrabutylammonium perchlorate (TBAP) and $FeCl_3 \cdot 6H_2O$ were purchased from commercial sources and used without further purification. The ligand 1,3–*bis*(2′–thiazolyl)iminoisoindoline (tia-BAIH) and [$Fe^{III}$(tia-ind)$Cl_2$] were synthesized according to known procedures [51].

### *2.2. Physical Characterization*

#### 2.2.1. Electrochemistry in Homogeneous Solution

Cyclic voltammetry (CV) and controlled potential electrolysis (CPE) were carried out on a BioLogic SP-150 galvano/potentiostat (Seyssinet-Pariset, France). To the solution of [$Fe^{III}$(tia-ind)$Cl_2$] in acetonitrile or acetone, water was added in 0–3 M concentration. Experiments were conducted under Ar with a standard three-electrode setup including a boron-doped diamond (BDD) working electrode (polished and conditioned before use), a Pt auxiliary electrode, and $Ag^+/Ag$ (0.01 M $AgNO_3$, 0.1 M TBAP/acetonitrile) reference electrode. The potentials were plotted against the ferrocenium/ferrocene ($Fc^+/Fc$) couple and measured in the same cell, under the same conditions. Electrolytic conductivity was determined by a calibrated Consort C533 multi-parameter analyzer (Turnhout, Belgium).

#### 2.2.2. Deposition of the Complexes on Semiconductor (ITO)

Indium tin oxide (ITO, ~100 nm thickness on glass slides) were purchased from Ossila Ltd. (Sheffield, UK). For the drop-casting the complex was dissolved in methanol in 3 mM concentration. Small aliquots (50–200 µL) were evenly layered onto the cleansed ITO by using a microsyringe. The solvent was evaporated and the solid was dried by infrared heating for 30 min (Figure 2).

**Figure 2.** Typical appearance of a drop-casted complex/indium tin oxide (ITO) sample.

#### 2.2.3. Electrochemistry with Drop-Casted Samples

All experiments were conducted in 0.2 M borate buffer at pH 8.3. Cleansed ITO with or without the complex ad-layer was set as the working electrode in a three-electrode setup (Pt auxiliary, separated by Nafion membrane in a different compartment, and Ag/AgCl reference, 3 M KCl), similarly to the reported method [11]. The evolution of $O_2$ was followed by gas chromatography (Shimadzu GC 2010 Tracera equipped with a BID detector (Shimadzu Co., Kyoto, Japan). Gas samples ($V$ = 200 µL) were taken from the headspace of the air-tight cell (the cell was filled with air of known composition as a blank) and injected through an injector unit into a circulation system (filled with 6.0 He) which contained a sampler loop. A circulating micropump was responsible for homogenization before the sample was let to the column through the inlet valve. The carrier and the plasma gas was 6.0 He. Calibration for sample volume and component sensitivity was done with the help of He gas and artificial air. The instrument settings were as follows: 40 mL/min total flow rate, 50 mL/min DCG

flow rate, 20 mL/min purge flow rate, $T_{col.}$ = 32 °C, $T_{det.}$ = 200 °C. An optical probe (NeoFox, Ocean Optics, Dunedin, FL, USA) was immersed into the electrolyte to detect the dissolved $O_2$ before and after electrolysis, which was additionally considered to calculate the Faraday efficiency.

#### 2.2.4. Scanning Electron Microscopy (SEM) and Energy Dispersive X-ray Spectroscopy (EDX)

These investigations were done on a Thermo Scientific Scios2 (Waltham, MA, USA) dual beam system equipped with an Oxford X-max$^n$ 20 SDD EDX (Abingdon, UK), 5 keV beam energy and process time 6 were applied, dead time was below 50%.

#### 2.2.5. X-ray Photoelectron Spectroscopy (XPS)

Surface composition of the sample deposited on the ITO electrode was determined by a KRATOS XSAM 800 XPS (Manchester, UK) instrument equipped with an atmospheric reaction chamber. Al K$\alpha$ characteristic X-ray line, 40 eV pass energy (energy steps 0.1 eV), and FAT mode were applied for recording the XPS lines of the Fe *2p* and *3p*, Sn *3d*, In *3d*, C *1s*, N *1s*, O *1s*, S *2p* and Cl *2p* photoelectrons, and the C *1s* binding energy at 284.8 eV was used as reference for charge compensation. The ratio of the elements at the surface was calculated from the integral intensities of the XPS lines using sensitivity factors given by the manufacturer.

#### 2.2.6. UV-Visible Spectrophotometry

Electronic absorption spectra were recorded on an Agilent Cary 60 spectrophotometer (Santa Clara, CA, USA) in quartz cuvettes at 25 °C. UV-vis titration of the complex in acetone, with water or $HClO_4$ were carried out in quartz cuvettes, and the solutions were stirred with a magnetic stirrer.

## 3. Results and Discussion

### *3.1. Structural Properties of [Fe$^{III}$Cl$_2$(tia-BAI)] and Its Behavior in Acetone*

The complex was synthesized and characterized earlier as part of a study on Fe$^{III}$ complexes exhibiting dioxygenase-like activity, e.g., capable of incorporating oxygen atoms into a catechol substrate [51]. We followed the synthetic procedure published there, which involves $FeCl_3 \cdot 6H_2O$ that is reacted with the ligand tia-BAIH in 1:1 ratio, in refluxing methanol under inert atmosphere resulting the pure [Fe$^{III}$Cl$_2$(tia-BAI)] (Figure 1) in ca. 65% yield. Note that our attempts to directly and selectively synthesize the aqua-Fe$^{III}$-BAI complex remained unsuccessful, most likely due to the water-insolubility of the ligand. Furthermore, ferrous or ferric salts with noncoordinating anions like perchlorate or triflate (which could allow instant solvation) tend to react with the ligand in as low as a 1:1 ratio in organic medium leading to the *bis*-chelate [Fe$^{II/III}$(BAI)$_2$]$^{0/+}$ as unwanted side-product [52], in addition to the mono-chelate compound. Apart from some exceptions [53] the isolation of the 1:1 complex from the product mixture would be complicated. Therefore, the readily available [Fe$^{III}$Cl$_2$(tia-BAI)] seemed to be a viable precursor from the viewpoint of the ease of its synthesis, even though chloride in principle might interfere with water oxidation as a competing ligand. As will be presented in more detail in Section 3.2, the chloride ligands, in fact, exchange with water thus allowing efficient water oxidation.

According to the reported single crystal structure of [Fe$^{III}$Cl$_2$(tia-BAI)] the complex is a five-coordinate, distorted trigonal bipyramidal with the tridentate, anionic tia-BAI$^-$ ligand occupying the two apical and one equatorial positions in meridional topology [51]. The central pyrrolic nitrogen atom (Figure 1) resides closer to the iron center than the two thiazolic nitrogen atoms (the Fe–N bond distances are 2.019(2) and 2.095(2) Å in avg., respectively) due to the greater Lewis basicity of the former, and the Fe–Cl distances are equally ~2.23 Å, altogether in agreement with a high-spin ferric center, in contrast with the homoleptic [Fe$^{III}$(tia-BAI)$_2$]$^+$ exhibiting shorter bond distances of ~1.95 and 2.00 Å, or similar *bis*-BAI$^-$ complexes with a low-spin ferric center [54].

Importantly, in the earlier report two electrochemically responsive species could be detected, when [$Fe^{III}Cl_2$(tia-BAI)] was dissolved in *N*,*N*-dimethylformamide solvent that has been attributed to the exchange of chloride to solvent upon reduction due to the more labile ferrous species [51]. We wished to examine the behavior of the complex in a noncoordinating solvent (miscible with water) in order to elucidate the redox properties of [$Fe^{III}Cl_2$(tia-BAI)] in itself. Therefore, the initial electrochemical investigations were performed in acetone.

Square wave voltammetry (SWV) from −0.7 to +1.6 V vs. $Fc^+$/Fc of the dichloride complex dissolved in acetone by using a boron-doped diamond (BDD) working electrode revealed three predominant redox events (Figure 3a). At −0.27 V vs. $Fc^+$/Fc a fully reversible redox transition is present that could be assigned as the $Fe^{3+/2+}$ transition of [$Fe^{III}Cl_2$(tia-BAI)]. Electrolytic conductivity of acetone with 1 mM complex (0.1 $\mu Scm^{-1}$) showed no significant increase compared to that of pure acetone (0.0 $\mu Scm^{-1}$), therefore this redox transition can be unequivocally associated with the nondissociated [$Fe^{III}Cl_2$(tia-BAI)] form. For comparison, the conductivity of the fully dissociating TBAP at 1 mM concentration is 152 $\mu Scm^{-1}$ under identical conditions.

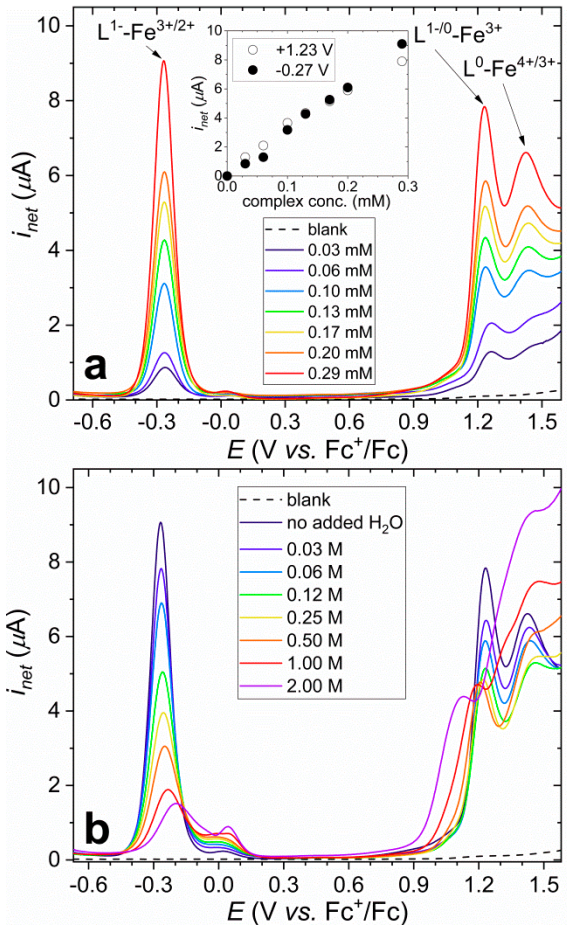


**Figure 3.** (**a**) Square wave voltammograms of [$Fe^{III}Cl_2$(tia-BAI)] dissolved in acetone at different concentrations ($L^{1-}$ stands for tia-$BAI^-$ in the assignments of the redox transitions), **inset**: $i_{net}$ peak currents as a function of complex concentration at −0.27 and +1.23 V vs. $Fc^+$/Fc; (**b**) changes in square wave voltammetry (SWV) current peaks upon addition of increasing amounts of water (see the legend) to the solution, $c$ = 0.29 mM for [$Fe^{III}Cl_2$(tia-BAI)]. WE: boron-doped diamond (BDD), RE: nonaqueous $Ag^+$/Ag, CE: Pt, Ar atm., 25 °C, 0.1 M tetrabutylammonium perchlorate (TBAP), SWV settings: $P_W$ = 80 ms ($f$ = 12.5 Hz), $P_H$ = 32 mV, $S_H$ = 4 mV.

Another quasi-reversible oxidation peak is present at +1.23 V vs. $Fc^+$/Fc (Figure 3a) that can be assigned as a ligand-based $1e^-$ oxidation of [$Fe^{III}Cl_2$(tia-BAI)], since the free tia-BAIH ligand also undergoes oxidation

at a somewhat lower potential (+1.13 V vs. $Fc^+/Fc$, Figure S1, in Supplementary Materials). The $i_{net}$ current at +1.23 V correlates with that of the $Fe^{3+/2+}$ transition and both are linearly dependent on the complex concentration (Figure 3a, inset). These observations suggest that both redox events can be associated with $[Fe^{III}Cl_2(tia\text{-}BAI)]$ and its consecutive $[Fe^{II}Cl_2(tia\text{-}BAI)]^{1-}/[Fe^{III}Cl_2(tia\text{-}BAI)]^0/[Fe^{III}Cl_2(tia\text{-}BAI^{\bullet})]^{1+}$ oxidation states. Finally, $[Fe^{III}Cl_2(tia\text{-}BAI^{\bullet})]^{1+}$ undergoes another oxidation step, which is irreversible and found at +1.43 V vs. $Fc^+/Fc$ (Figure 3a). This transition we tentatively associate with the oxidation of the $Fe^{III}$- to $Fe^{IV}$-center, which probably triggers a chemical reaction step involving the chloride ligand.

### *3.2. Addition of Water to the Solution of $[Fe^{III}Cl_2(tia\text{-}BAI)]$ in Acetone*

The above-detailed electrochemical transitions for $[Fe^{III}Cl_2(tia\text{-}BAI)]$ in acetone undergo fundamental changes when water is added to the solution (Figure 3b). All current peaks that were originally present (Figure 3a) decrease simultaneously as an increasing amount of water is added, roughly up to 0.12 M. Beside the $[Fe^{II}Cl_2(tia\text{-}BAI)]^{1-}/[Fe^{III}Cl_2(tia\text{-}BAI)]^0$ transition at −0.27 V a new current wave occurs at above 0 V vs. $Fc^+/Fc$, but the potential for its $i_{net}$ current maximum ($E_{net}$) changes with the water/complex ratio. At higher concentrations of water (0.12 to 2.0 M) a new current peak can be identified at +0.04 V vs. $Fc^+/Fc$. Note that increasing the proportion of water to a certain level in the mixture causes slow precipitation of a solid, therefore investigations were limited to a certain concentration regime only. Based on the above observations it is reasonable to assume that $[Fe^{III}Cl_2(tia\text{-}BAI)]$ is transformed to $[Fe^{III}Cl(H_2O)(tia\text{-}BAI)]^{1+}$ and $[Fe^{III}(H_2O)_2(tia\text{-}BAI)]^{2+}$, or the singly deprotonated $[Fe^{III}(OH)(H_2O)(tia\text{-}BAI)]^{1+}$ via stepwise $Cl^-$ to $H_2O$ ligand exchange reaction upon addition of water. (The existence of six-coordinate variants with both chloride and aqua ligands cannot be excluded. However, exact evaluation of the solution equilibria and addressing the five- or six-coordinate specification would be ambiguous at this point, therefore, in the course of further discussions only the above assignments are considered for the sake of simplicity. As it will be explained later, from the viewpoint of water oxidation the absence of chloride and the presence of at least two adjacent coordinated water molecules are the most relevant pieces of information. Although chloride as an inner-sphere ligand may have role in catalysis [30], the investigation of this aspect is beyond the scope of this study.)

The conductivity of the solution should be sensitive to the presence of ionic species resulting from the proposed ligand exchange. Indeed, when water is added in 3.0 M concentration ($x_{water}$ = 0.19) to the solution of $[Fe^{III}Cl_2(tia\text{-}BAI)]$ (1 mM) the conductivity increases from 0.1 to 15.6 $\mu Scm^{-1}$ (in contrast, addition of water to pure acetone causes no change in conductivity). The increased conductivity can be clearly associated with the presence of ionic species, uncoordinated $Cl^-$, the cationic forms of the aqua complexes and $H_3O^+$ that may be present from the acidic proton of the $Fe^{III}$-$OH_2$ moiety (according to p$K_a$ values of acetone and water the latter will be the proton acceptor [55]). However, its modest value suggests that only a low proportion of chloride is dissociated [56] in the ferric state. On the other hand, the thorough changes in the $Fe^{3+/2+}$ current peaks upon water addition in Figure 3b indicate that the reduction of the metal center facilitates ligand exchange and pushes the equilibrium towards aqua-complex formation (Scheme 1).

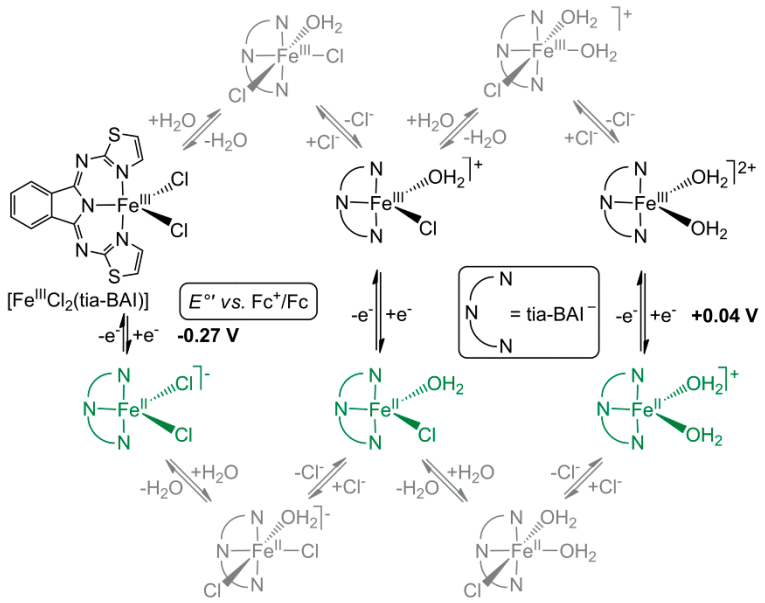


**Scheme 1.** Proposed ligand exchange steps leading from $[Fe^{III/II}Cl_2(tia\text{-}BAI)]^{0/-}$ to $[Fe^{III/II}(H_2O)_2(tia\text{-}BAI)]^{+/0}$.

The electronic spectrum of the complex (like the redox transitions detected in SWV) also undergoes changes, when water is added (Figure 4a). In addition to the high intensity intra-ligand charge transfer (ILCT) bands originating from the $\pi$–$\pi^*$ transitions of the coordinated BAI at 392, 413, and 441 nm, ligand-to-metal charge transfer (LMCT) bands are also present above 480 nm with lower intensity. Addition of water results in a bathochromic shift in the ILCT bands (solvation), moreover, the LMCT bands are affected, too, that indicates a change in the ligand configuration (the LMCT bands somewhat overlap with the high intensity ILCT absorptions and therefore occur as ill-defined shoulder).

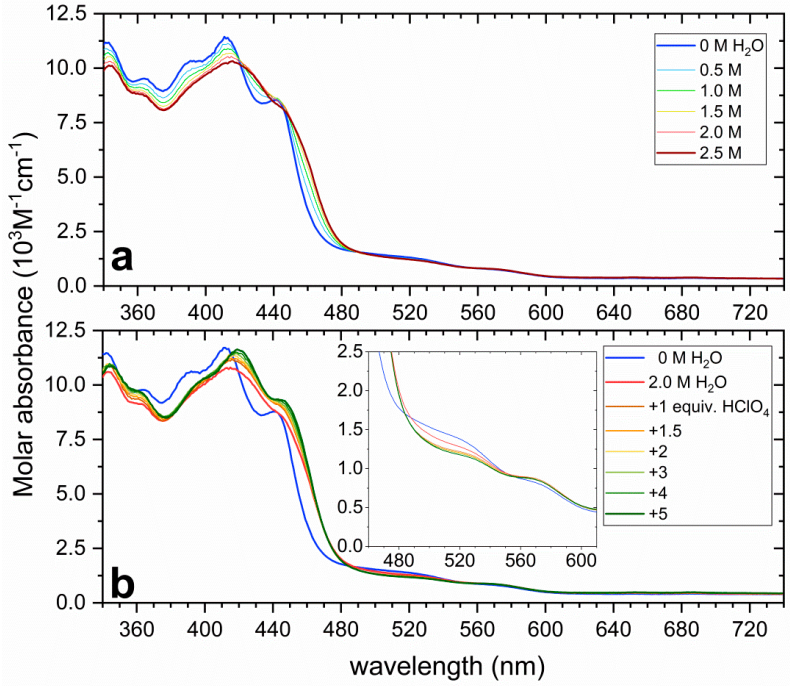


**Figure 4.** (**a**) UV-visible spectra of the $[Fe^{III}Cl_2(tia\text{-}BAI)]$ complex in acetone recorded in an $l$ = 1 cm quartz cuvette at different concentrations of water; (**b**) the effect of acid ($HClO_4$) on the electronic spectrum of the $[Fe^{III}Cl_2(tia\text{-}BAI)]$ + water mixture in acetone (the **inset** shows the 460–610 nm range magnified). Conditions: $c$ = 0.2 mM in 3 mL acetone, 25 °C, under air.

The shift in the isosbestic points (in the vicinity of 420, 440, and 490 nm) indicate the presence of more than two absorbing species that would be consistent with the occurrence of the proposed $[Fe^{III}Cl(H_2O)(tia\text{-}BAI)]^{1+}$, $[Fe^{III}(H_2O)_2(tia\text{-}BAI)]^{2+}$ and/or $[Fe^{III}(OH)(H_2O)(tia\text{-}BAI)]^{1+}$ forms in addition to the initial $[Fe^{III}Cl_2(tia\text{-}BAI)]$. Addition of the strong acid $HClO_4$ in the presence of 2 M water in acetone shifts the ILCT bands to lower energy along with some increase in absorbance (Figure 4b). In the LMCT region around 520 nm the greatest change takes place as soon as upon addition of the 1st equiv. of $HClO_4$ (Figure 4b, inset, compare the red and the orange spectra) supporting the occurrence of a $Fe^{III}$-L to $Fe^{III}$-LH protonation step and the associated change in the LMCT band energy.

Taken together the observations by SWV, electrolytic conductivity and UV-vis spectrophotometry in a homogeneous solution the coordination of water to the ferric center can take place *via* the exchange with chloride. Detailed NMR investigations on high-spin five-coordinate $Fe^{II}$- and $Co^{II}$-BAI complexes revealed an associative exchange mechanism for the rearrangement of Cl-M-solvent units through a six-coordinate transition state [57]. Accordingly, we suggest a similar addition-elimination mechanism for the formation of $[Fe^{III}Cl(H_2O)(tia\text{-}BAI)]^{+}$ and $[Fe^{III}(H_2O)_2(tia\text{-}BAI)]^{2+}$, moreover, for the complex forms involving $Fe^{II}$ (Scheme 1).

### *3.3. Electrocatalytic Water Oxidation in Water/Acetone with $[Fe^{III}Cl_2(tia\text{-}BAI)]$*

The current peaks in SWV at +1.23 V and +1.43 V vs. $Fc^{+}$/Fc originally present for $[Fe^{III}Cl_2(tia\text{-}BAI)]$ gradually give place to new current peaks at +1.12 and +1.46 V vs. $Fc^{+}$/Fc when water is added to the solution (Figure 3b, yellow, orange, red and purple SWVs). This can be explained by means of $Cl^{-}$ to $H_2O$ ligand exchange, too (Figure 3b). When $H_2O$ is present in higher amounts it can act as a ligand and proton acceptor to furnish predominantly the $[Fe^{III}(OH)(H_2O)(tia\text{-}BAI)]^{1+}$ equilibrium form. We assume that the current peak at +1.12 vs. $Fc^{+}$/Fc ($c_{H2O}$ = 3 M) comes from the ligand-associated $1e^{-}$ oxidation of $[Fe^{III}(OH)(H_2O)(tia\text{-}BAI)]^{1+}$ to $[Fe^{III}(OH)(H_2O)(tia\text{-}BAI^{\bullet})]^{1+}$ (proton-coupled electron transfer can be also operational for the oxidation of $[Fe^{III}(H_2O)_2(tia\text{-}BAI)]^{1+}$ to $[Fe^{III}(OH)(H_2O)(tia\text{-}BAI^{\bullet})]^{1+}$), and the peak at +1.46 V vs. $Fc^{+}$/Fc can be associated with a subsequent oxidation to $[Fe^{IV}(O)(H_2O)(tia\text{-}BAI^{\bullet})]^{1+}$ (Scheme 2, on the right). This species could be thermodynamically competent in the water nucleophilic attack (WNA) reaction. Indeed, cyclic voltammetry in the presence of water reveals catalytic increase in the current at more positive potentials (*vide infra*, the CVs beyond the +1.3 V potential range of the re-dissolved samples after long term electrolysis producing $[Fe^{III}(H_2O)_2(tia\text{-}BAI)]^{1+}$, in Section 3.4, see also Figure S2 in Supplementary Materials).

The WNA step, i.e., the chemical reaction of $H_2O$ by $[Fe^{IV}(O)(H_2O)(tia\text{-}BAI^{\bullet})]^{1+}$ is proposed to yield $[Fe^{IV}(OOH)(H_2O)(tia\text{-}BAI^{\bullet})]^{1+}$ by the dissociation of one proton (Scheme 2). This step is most likely assisted by H-bonding interaction with the adjacent aqua ligand considering the results of a detailed computational work by Lloret-Fillol et al. [58], where the adjacent hydroxide ligand was held responsible for directing the $H_2O$ substrate molecules. By exchanging $H_2O$ to $D_2O$ a kinetic isotope effect (KIE = ${i_{cat}}^2(H_2O)/{i_{cat}}^2(D_2O) = k_{cat}(H_2O)/k_{cat}(D_2O)$) of ~1.4 can be estimated based on the CVs in the catalytically enhanced current range (> +1.3 V, see Figure S2).

This KIE value is lower than what we found earlier for a single-site Fe molecular electrocatalyst exhibiting a proposed '$Fe^{V}(O)(OH)$' active species (the KIE was 2.0) [11], and its value indicates a reorganization of the O–H bonds in the a rate-limiting step with bulk water as the proton acceptor [59] (consistently with the proposed WNA step in Scheme 2).

In contrast, KIE was absent for chemically activated catalysts by using $Ce^{IV}$ as the oxidant [60]. In the presence of N4 ligands an $Fe^{IV}(O)(\mu\text{-}O)\text{–}Ce^{IV}$ adduct could be detected, and the $Fe^{V}(O)(OH)$ active form was generated by an inner sphere electron transfer mechanism [39,60]. This species was suggested to react with $H_2O$ in the rate-determining step resulting in $Fe^{III}(OOH)(OH_2)$, thus reorganization of the O–H bonds and KIE were minimal [27].

In our case, the further oxidation steps that close the proposed catalytic cycle will be discussed later, in light of the re-dissolution test and surface analysis of the heterogenized samples. It is to note here that similar results could be achieved in propylene carbonate (PC) or acetonitrile (ACN) solvent,

since both are miscible with water. However, in the former case the solubility of the compound is lower, while in the latter, the coordination of ACN molecules complicates analysis of redox transitions.

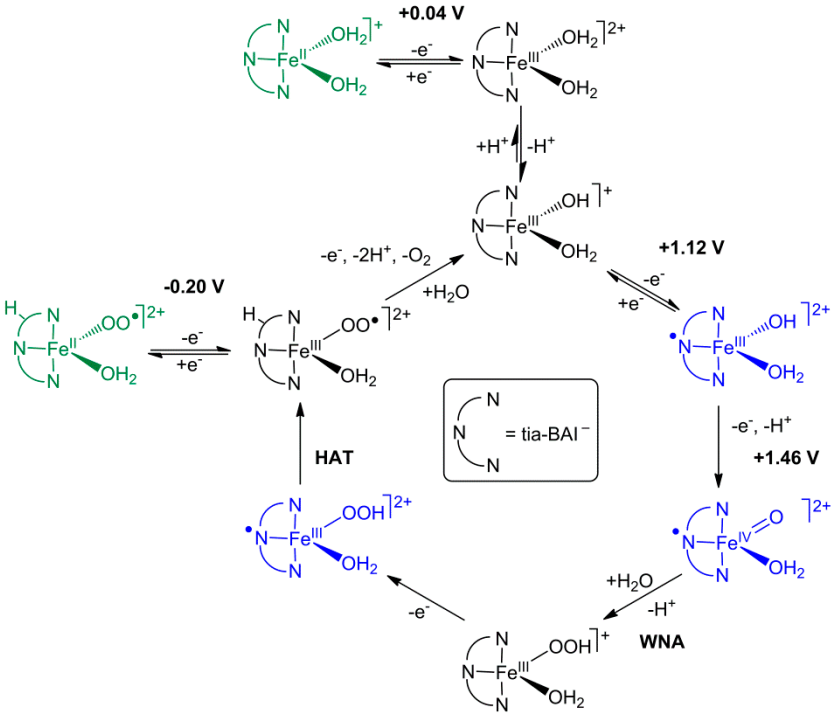


**Scheme 2.** Proposed mechanism for the water oxidation electrocatalysis by the $[Fe^{III}(H_2O)_2(tia\text{-}BAI)]^{1+}$ active complex form. Intermediates with tia-BAI$^{\bullet}$ radical appear in blue. The $Fe^{II}$-complex in green is the $Fe^{II}$ form of the suspected intermediate detected by cyclic voltammetry (CV), as shown in Figure 9c. The potential values are given vs. Fc and apply in water/acetone.

### *3.4. Characterization of the Complex as a Solid Ad-Layer on Indium Tin Oxide*

The solid precatalyst complex with its pincer ligand is practically insoluble in water fostering its deposition from an organic solvent to ITO/glass and subsequent utilization as an anode in aqueous electrolyte. Earlier, simple drop-casting of an Fe-complex in methanol was found suitable and convenient to fabricate ad-layers that could be applied in controlled potential electrolysis (CPE) experiments [11]. Like in our earlier study, we hypothesized that the self-supporting ad-layer could be formed starting from $[Fe^{III}Cl_2(tia\text{-}BAI)]$ on ITO and the exchange of the chloride ligands with solvent molecules observed in water/acetone mixtures for $[Fe^{III}Cl_2(tia\text{-}BAI)]$ could help grafting of the catalytic activity of the Fe-(tia-BAI) moieties to the solid electrode-aqueous electrolyte interface.

Methanol was selected, because our previous study revealed that a more stable layer can be obtained by using this solvent instead of acetonitrile, acetone, or propylene carbonate. In the case of $[Fe^{III}Cl_2(tia\text{-}BAI)]$, the conductivity of its 1 mM solution in methanol was 83.7 $\mu Scm^{-1}$, indicating the dominance of an ionic $Fe^{III}$-complex. SWV showed the presence of a single, quasi-reversible $Fe^{3+/2+}$ redox couple at +0.08 V vs. $Fc^{+}/Fc$ (Figure 5).

This is similar, but not identical to the redox potential found at +0.04 V for the sample redissolved from ITO after long-term electrolysis (*vide infra*), moreover, what we detected in water/acetone mixtures (Figure 3b), and associated with water addition followed by chloride elimination (Scheme 1). Therefore, it hints the existence of a methanol-coordinated complex. In turn, when copious amounts of water are added to the solution of the complex in methanol, the $Fe^{3+/2+}$ redox couple occurs at +0.04 V vs. $Fc^{+}/Fc$ (Figure 5) that supports the hypothesis of an easy access to the aqua-complex in this medium (note that the solvent window of methanol in electrochemistry did not allow investigating the more positive potential region to detect catalytic events).

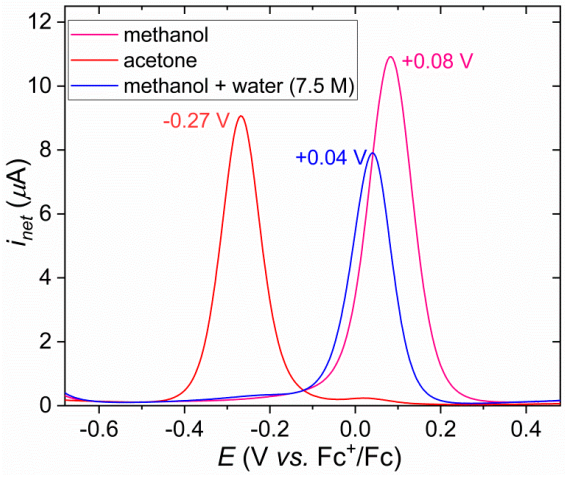


**Figure 5.** Square wave voltammograms of [$Fe^{III}Cl_2$(tia-BAI)] dissolved in acetone (red, $c$ = 0.29 mM), methanol (pink, $c$ = 0.75 mM), and 3 M water/methanol mixture (blue, $c$ = 0.75 mM). WE: BDD, RE: nonaqueous $Ag^+$/Ag, CE: Pt, Ar atm., 25 °C, 0.1 M TBAP, SWV settings: $P_W$ = 80 ms ($f$ = 12.5 Hz), $P_H$ = 32 mV, $S_H$ = 4 mV.

Overall, our results suggest that methanol favors the dissociation of the chloride ligands, thus the layered crystalline solid (the SEM pictures are seen in Figure 6a) should consist of [$Fe^{III}Cl_{(2-x)}$(solvent)$_x$(tia-BAI)](Cl)$_x$ (x = 1, or 2) species, where $H_2O$ molecules from the aqueous electrolyte can generate the proposed [$Fe^{III}(H_2O)_2$(tia-BAI)]$^{2+}$ active form. Indeed, this coating is catalytically active and produces $O_2$ (vide infra), while layering from acetone results in very small activity thus underlining the pivotal role of the choice of solvent for drop-casting.

The surface morphology of the freshly drop-casted complex/ITO electrode (0.31 μmol [$Fe^{III}Cl_2$(tia-BAI)] in 100 μL methanol, spread over 2.37 cm$^2$ ITO, Figure 2) was analyzed by scanning electron microscopy (SEM), and its composition by energy dispersive X-ray spectroscopy (EDX, Figure 6a), in addition to X-ray photoelectron spectroscopy (Tables 1 and S1, Figures 7 and S3). The SEM view of the freshly drop-casted complex/ITO shows submicron size crystallites attached to the ITO surface in a relatively even distribution. The SEM image at ×500 magnification in Figure 6a (50 μm scale bar) illustrates a typical arrangement, i.e., areas covered by crystallites directly attached to ITO alternating with thicker, microporous layers of crystals (darker patches). The elemental composition by EDX is consistent with the expected presence of C, N, O, S, Cl, and Fe for [$FeCl_2$(tia-BAI)], or the derived [$Fe^{III}Cl_{(2-x)}$(solvent)$_x$(tia-BAI)](Cl)$_x$ complex and some contribution from In and Si (Figure 6a) originating from the support. The porous structure of the thicker patches is expected to increase durability of the layer, since it may help the $O_2$ bubbles leaving from the surface.

The XPS analysis of the as-prepared complex/ITO sample reveals the chemical composition of the surface layer that can make contact with the liquid phase, and is thought to be responsible for the electrocatalysis. The surface ratio of the elements (Table 1) confirms the presence of the expected elements for the precursor (Fe, C, N, O, S, and Cl), beside Sn and In from ITO. According to the results the surface atomic ratios for the sample are Fe:C:N:S = 1:19.5:5.5:1.8 (expected, 1:14:5:2 for [$FeCl_2$(tia-BAI)]) indicates that the Fe:tia-BAI ratio is 1:1, with some excess of C. Although it is tempting to say that excess C originates from methanol molecules coordinated to iron, it is rather likely that adventitious C is observed by XPS. The Fe:Cl ratio is 1.4 (Table 1), which is lower compared to the expected value of 2 for the original precursor complex. This ratio is already indicative of the dissociation of chloride from the coordination sphere and its partial loss.

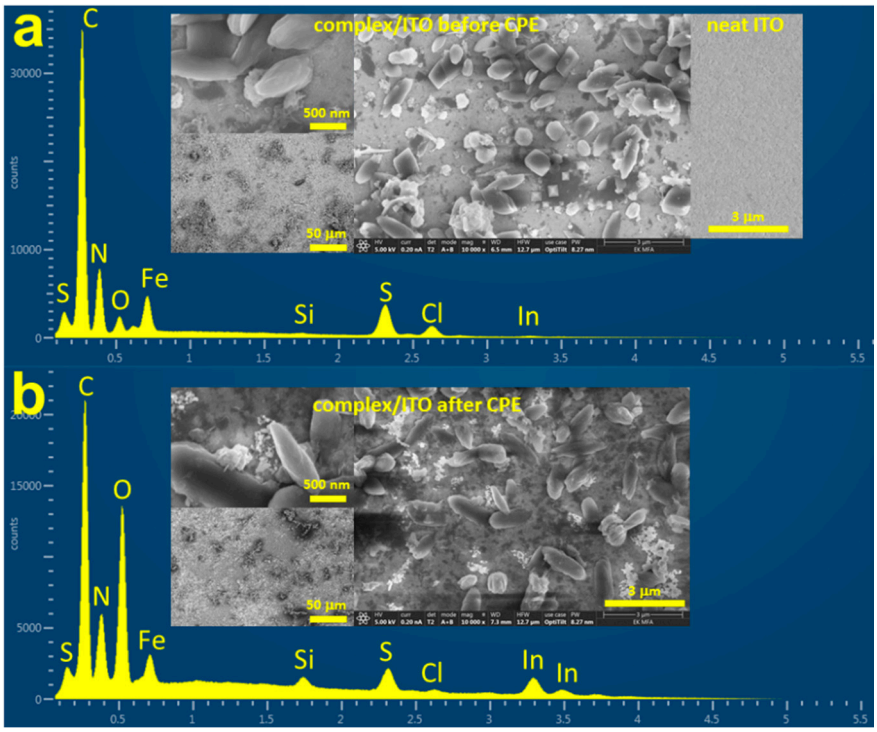


**Figure 6.** (**a**) EDX spectrum of an as-prepared complex/ITO sample (0.31 µmol over 2.37 $cm^2$), inset: SEM images of the sample at ×500, ×10,000, and ×50,000 magnification and the neat ITO surface (×10,000); (**b**) EDX spectrum of the sample after 4.5 h controlled potential electrolysis (CPE) at +1.4 V vs. Ag/AgCl in 0.2 M borate buffer at pH 8.3 (see Figure 8 and discussion for more details), inset: SEM images of the sample after electrolysis at ×500, ×10,000, and ×50,000 magnification. Experimentals for SEM: 5 kV beam accelerating voltage, 0.20 nA probe current, Everhart-Thornley detector, operation for secondary electron, 6.5 mm working distance (7.3 mm for the sample after electrolysis). The detection mode was optimized for horizontal plane with short working distance. EDX: energy dispersive X-ray spectroscopy.

**Table 1.** XPS surface composition of as-prepared complex/ITO drop-casted from methanol and the same sample after 4.5 h of CPE at +1.4 V vs. Ag/AgCl.

| Element | Surface Ratio (at.%) | |
|---|---|---|
| | Fresh | After CPE |
| Fe | 2.81 | 2.01 |
| O | 12.34 | 17.15 |
| N | 15.53 | 15.09 |
| C | 54.76 | 53.97 |
| Cl | 3.90 | 0.24 |
| S | 5.05 | 4.86 |
| Sn | 0.64 | 0.68 |
| In | 4.97 | 6.00 |
| *N/Fe* | *5.5* | *7.5* |
| *Cl/Fe* | *1.4* | *0.12* |

The Fe 2p peaks exhibit satellite features indicating high-spin $Fe^{III}$ (Figure 7a). The splitting energy, $\Delta$ = B.E.(Fe $2p_{1/2}$)—B.E.(Fe $2p_{3/2}$) = 13.2 eV, is also in accordance with a high-spin ferric state with increased spin-orbit coupling [61], or $\Delta$ values typically observed for spin-crossover complexes [62,63]. The fitting of the Fe 2p multiplet ('Fe 2p 1-3') and the shake-up satellite ('Fe 2p 4') is illustrated in Figure 7a, the selected binding energy data from the fitted component peaks are listed in Table S1. The analysis of the Cl 2p peaks (Figure 7b) reveals that only a minor part of the remaining chloride is

bound to iron (doublet peaks 'Cl 2p 3-4' in Figure 7b) and the majority of it is uncoordinated (doublet peaks 'Cl 2p 1-2'). This result is in accordance with the outer sphere presence of chloride and the predominance of a $[Fe^{III}(solvent)_2(tia\text{-}BAI)](Cl)_2$ form.

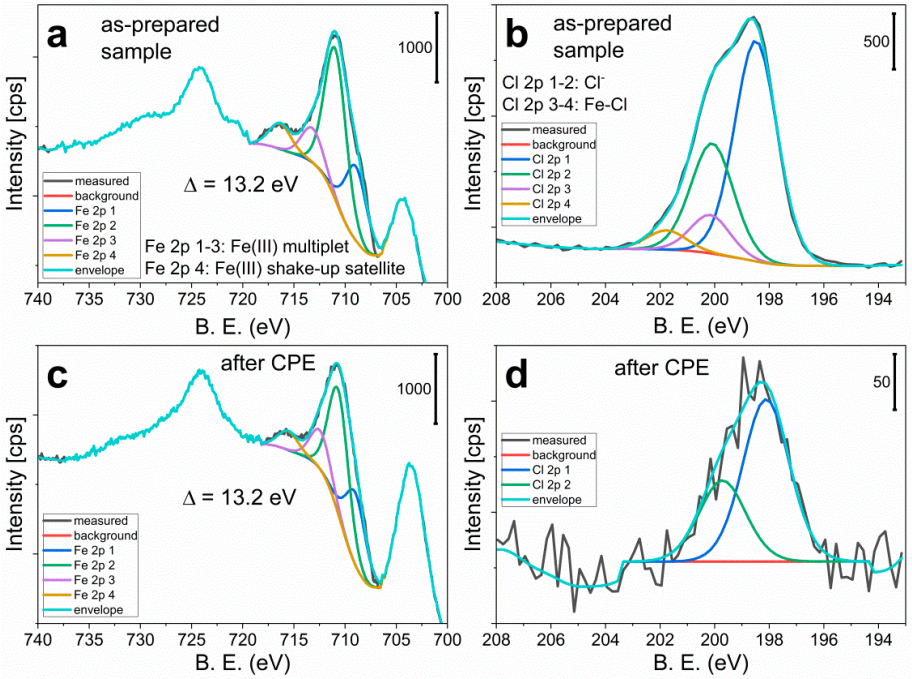


**Figure 7.** (**a**) The Fe 2p and (**b**) the Cl 2p binding energy region of XP spectra of the as-prepared complex/ITO with the fitted components; (**c**,**d**) the corresponding spectra after CPE (Figure 8). For discussion see the text, for data see Tables 1 and S1.

The N atoms in the ancillary ligand tia-BAI are found in different environments, including uncoordinated exocyclic imine groups (C=N–C) and coordinated heterocyclic donor groups (Fe–$N_{hc}$). Fitting of the N 1s peak shows two components at 398.9 and 400.9 eV binding energy (Figure S3, see Supplementary Materials). The former, major component can be assigned as an unresolved mix of the coordinated Fe–$N_{hc}$ donor atoms and the exocyclic C=N–C imine moieties. In metal phthalocyanines (MPc-s), a family of compounds closely related to our complex, it is known that despite their nonequivalence the 1s core levels of the metal-coordinated and iminic N atoms lie close in energy [64,65]. This normally leads to an unresolved, single N 1s core level peak, like in our case. The minor, blue-shifted peak at ~2 eV higher binding energy can be tentatively associated with some hydrogenated N atoms, based on the DFT calculations by Sarasola et al. [65]. This allows to presume the occurrence of $Fe(tia\text{-}BAIH)^{3+}$ moieties, but a minimal demetalation of the ligand after its hydrogenation cannot be excluded, as well (*vide infra*). The S $2p_{1/2}$ and S $2p_{3/2}$ doublet at 164.4 and 165.6 eV, respectively (Figure S3) is associated with the $S_{tia}$ atoms of the ligand. According to the presence of a doublet at 167.0 and 168.2 eV (Figure S3, see Supplementary Materials) a small amount of sulfone groups are present, probably formed by the oxidation of the thiazole units at the ITO surface.

### *3.5. Application of the Complex in Water Oxidation as Solid Ad-Layer on Indium Tin Oxide Anode, and Follow-Up Analysis*

Following its surface analysis as detailed in the previous section, the drop-casted complex/ITO electrode (0.31 μmol complex spread over 2.37 $cm^2$ ITO) was applied in controlled potential electrolysis (CPE), in borate buffer at pH 8.3. The potential of the working electrode was set to +1.4 V vs. Ag/AgCl, the electrolyte was slowly stirred, and the electrolyte containing the counter electrode was connected through a Nafion membrane. Figure 8a shows the current and charge as a function of CPE duration.

After an initial drop the current is steady for ca. 1 hour. In this period $\Delta Q$ is ~4 C and bubble formation is continuous.

The steady period is followed by a slow decrease in the current from 1.7 to 1.2 mA, until the stop of CPE after 4.5 h (the current on plain ITO working electrode is negligible under the same conditions [11]). The evolution of oxygen gas was followed by GC analysis of headspace samples taken after ~2 and ~4 h, finally, after stopping CPE (Figure 8b, the cell was purged with air of known composition prior to CPE). In this experiment roughly 2 $cm^2$ of the complex/ITO anode, i.e., 0.26 μmoles of the complex was immersed into the solution. After the pass of 24.34 C corresponding to 252 μmoles of electrons (considering a $4e^-$ process and 100% Faraday efficiency, this means 63 μmoles of produced $O_2$ as theoretical maximum) 50.4 μmol $O_2$ could be detected by GC from the headspace. Based on GC detection this means an overall turnover number (TON) of 193 and a turnover frequency (TOF) of 0.012 $s^{-1}$, by 80% Faraday efficiency (Figure 8c) at $\eta$ = 0.86 V ($\eta = E_{WE} + E(Ag/AgCl) - E°(O_2/H_2O) + 0.059$ pH). However, the amount of dissolved $O_2$ in the electrolyte also increased by 8.9 μmol by the end of CPE (single-point detection before and after CPE by an optical probe [11]), which allows us to estimate overall 94% Faraday efficiency, a TON of 228, and a TOF of 0.014 $s^{-1}$. However, this gives only a lower limit for TON and TOF, since not all the immobilized complex contributes equally to catalysis.

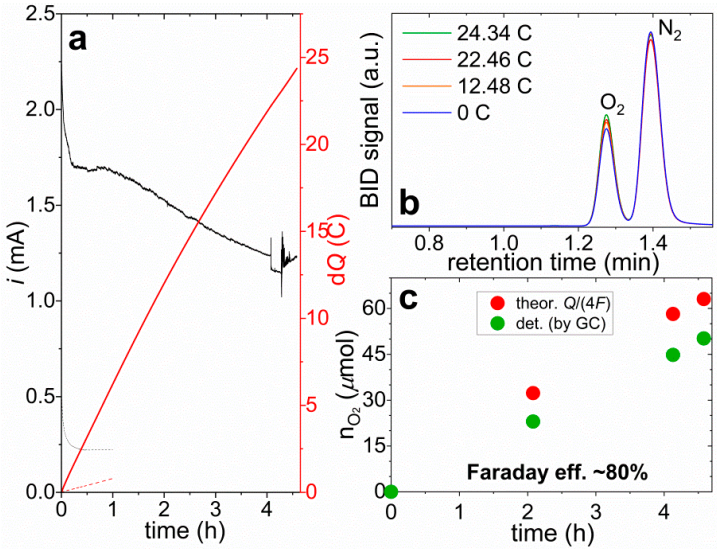


**Figure 8.** (**a**) Current (black) and charge (red) during controlled potential electrolysis performed at +1.4 V vs. Ag/AgCl for over 4.5 hours in 0.2 M borate buffer, at pH 8.3 by using an ITO working electrode drop-casted with the complex (0.31 μmol over 2.37 $cm^2$, ~2 $cm^2$ was dipped into the electrolyte, dashed lines show the current and charge on pristine ITO), Pt counter electrode separated by a Nafion membrane; (**b**) gas chromatograms of headspace samples taken at different stages of electrolysis, the peak of $O_2$ comes first, $N_2$ second, the cell was filled with air of known composition; (**c**) comparison of the theoretical and detected $O_2$. For results see the article text.

The surface morphology of the complex/ITO after CPE showed changes according to the SEM images (Figure 6b). Areas where crystallites remained attached to the ITO surface exhibited similar features like on the as-prepared surface. Thicker layers of crystals (darker patches) were still observed, too, but from some patches the original crystallites were missing. The loss of the crystallites of the catalyst from the ITO support may be partly responsible for the gradual decrease of current in the course of CPE. On the other hand, the composition by EDX (Figure 6b) indicates the almost total absence of $Cl^-$ and an increase in the O-content (along with that of in which should be the result of the catalyst-free patches). The elemental composition by EDX (Figure 6b) suggests that the outer-sphere counter-ions are almost completely exchanged from beside the cationic $Fe^{III}(solvent)_2$(tia-BAI) assemblies. XPS also confirmed that less than 7% of $Cl^-$ remained in the layer, indicating that the contact with the electrolyte and CPE induces ion exchange in the solid phase. Interestingly, the proportion and atomic% of

elements (C, N, and S) that are characteristic of the tia-BAI$^-$ ligand are hardly changed (Table 1). This may suggest two phenomena, both of which may play important roles in the course of CPE. Firstly, the lattice energy of the crystalline complex should be supported by strong $\pi$-stacking between the tia-BAI$^-$ ligands that is a well-known phenomenon [66,67], and in our case it aids the stabilization of a robust catalyst layer. Secondly, despite the absence of crystallites in patches (Figure 6b) the unchanged atomic% of C, N, and S in the outermost <3 nm layer (the maximum depth of XPS detection in our case) indicates the existence of a quasi-monolayer of complex at the ITO surface. Importantly, the atomic% for Fe is lower roughly by 30% than it was before CPE. In light of the above discussion we think that the major route of losing the WOC activity should be the leaching of $Fe^{3+}$ ions from the complex, leaving the ligand behind in the solid phase. One more change in the XP spectrum is worth mentioning that may shade the above deactivation mechanism. The blue-shifted peak for the N 1s at 401.1 eV (Table S1) associated with hydrogenated N atoms in $Fe^{III}$(tia-BAIH)$^{3+}$ moieties is increased in intensity on the expense of the main N 1s peak (Figure S3, see Supplementary Materials). This suggests that demetalation might be induced by a hydrogen atom transfer (HAT) to the ligand as side-reaction that would be in line with a proposed HAT step of the catalytic mechanism in Scheme 2.

In order to analyze the complex layer in more depth after CPE, a re-dissolution experiment was carried out. In this case CPE was performed in a standard 3-electrode cell at +1.4 V vs. Ag/AgCl, in borate buffer at pH 8.3, with an ITO support drop-casted with 0.35 µmol complex (0.15 µmol/cm$^2$). A CV scan prior to CPE revealed the $Fe^{3+/2+}$ redox couple for the complex adsorbate at +0.65 V on the anodic, and +0.37 V on the cathodic branch, while the onset potential of catalysis occurred at +1.15 V (Figure 9a). (Note that upon multiple scans to turning potentials more negative than the $Fe^{3+}$-to-$Fe^{2+}$ reduction a parallel and proportional decrease occurs in the $Fe^{3+/2+}$ redox peaks and the catalytic current. This indicates that the reduction-oxidation cycle of the iron center accelerates demetalation in the case of the drop-casted complex.)

The duration of CPE was set to ~1.5 h ($\Delta Q$ ~ 7 C) in order to avoid significant demetalation, but maximize the chloride dissociation, and the complex/ITO was then rinsed with acetone in an ultrasonic bath for 5 minutes. The color of acetone quickly became brownish-yellow and only a small remnant of the complex coating was visible on the ITO surface. The SWV with a BDD working electrode of the re-dissolved sample ($c_{max}$ ~ 0.09 mM) revealed a single, reversible $Fe^{3+/2+}$ redox transition at +0.04 V vs. $Fc^+$/Fc (Figure 9b), which matches with the redox peak associated with a proposed [$Fe^{III}(H_2O)_2$(tia-BAI)]$^{2+}$ in the homogeneous system (Figure 3 and Scheme 2). The current peak at +1.16 vs. $Fc^+$/Fc and the follow-up wave shows good agreement with the transitions assigned as the ligand-associated 1e$^-$ oxidation to [$Fe^{III}$(OH)($H_2O$)(tia-BAI$^\bullet$)]$^{1+}$ and a concomitant oxidation to [$Fe^{IV}$(O)($H_2O$)(tia-BAI$^\bullet$)]$^{1+}$ (Figure 3b and Scheme 2).

Note that a shoulder preceding the peak at +1.16 V indicates the presence of some free ligand and supports our hypothesis of demetalation upon CPE. Addition of water (1 M) to this solution yields increased current in the electrocatalytic regime (Figure 9b, dashed red curve), thus confirms that the re-dissolved species is responsible for WOC. The latter fact is also apparent from the multiple-cycle CV recorded at 100 mVs$^{-1}$ scan rate in the same solution (Figure 9c).

Surprisingly, in addition to the features that are present in the SWV, a reversible redox couple occurs roughly at −0.2 V vs. $Fc^+$/Fc starting from the 2nd cycle, i.e., after the electrode is polarized through the potential range of electrocatalysis. An enlarged view is shown in the inset of Figure 9c of the 1st (dashed green line) and the 2nd cycle of CV recorded at 200 mVs$^{-1}$ (green line). If the scan rate is lowered this reversible feature will be absent, and only the $Fe^{3+/2+}$ redox couple is seen that has been associated with the [$Fe^{III}(H_2O)_2$(tia-BAI)]$^{2+}$ complex (Figure 9c, inset). This suggests that an intermediate species is detected at −0.2 V vs. $Fc^+$/Fc, which is generated in the course of electrocatalysis. Based on its redox potential, we tentatively assign this transition as the $Fe^{3+/2+}$ redox couple of a proposed intermediate, possibly [$Fe^{III}$(OO$^\bullet$)($H_2O$)(tia-BAIH)]$^{2+}$ that might be generated from [$Fe^{III}$(OOH)($H_2O$)(tia-BAI$^\bullet$)]$^{2+}$ by a HAT step from the hydroperoxide to one of the uncoordinated iminic N atoms of the tia-BAI$^\bullet$ ligand, as is illustrated in Scheme 2 (see also the discussion about XPS N 1s binding energy data). In the

proposed mechanism a concomitant transformation of $[Fe^{III}(OO^{\bullet})(H_2O)(tia\text{-}BAIH)]^{2+}$ regenerates $[Fe^{III}(H_2O)_2(tia\text{-}BAI)]^{2+}$ thus closing the catalytic cycle with the involvement of an $H_2O$ molecule. We think that the detection of a relatively short-lived intermediate is possible because of the depletion of water from the diffusion layer near the BDD electrode. Note that this is only one possible assignment and further evidence (either experimental or theoretical) is required to confirm or exclude the existence of the peroxo species.

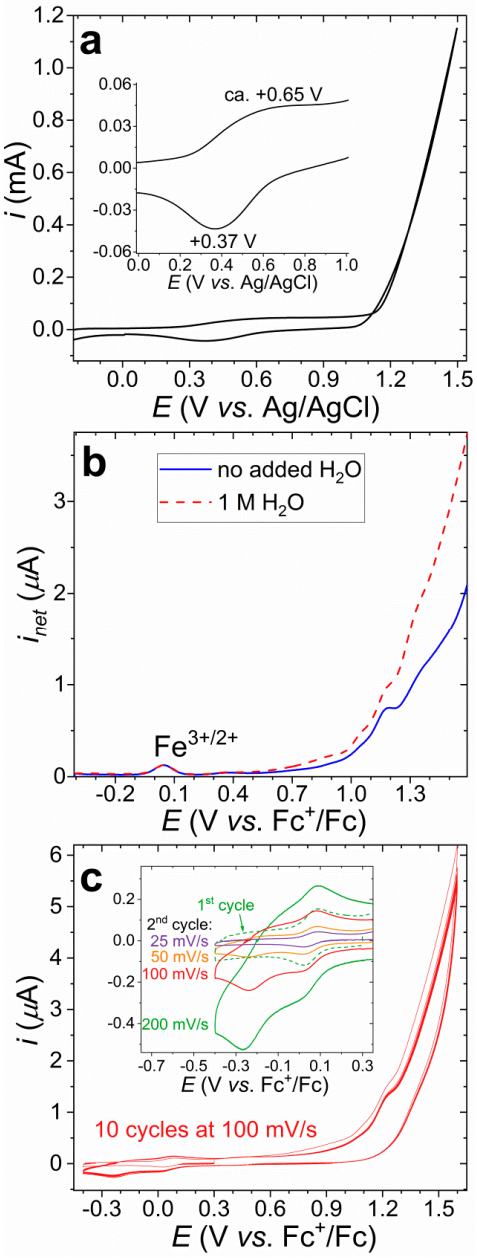


**Figure 9.** (**a**) First CV scan of a complex/ITO electrode (0.35 μmol complex drop-casted from methanol to 2.37 $cm^2$ ITO) at 100 $mVs^{-1}$ in 0.2 M borate buffer at pH 8.3, **inset**: magnified view of the $Fe^{3+/2+}$ redox couple; (**b**) SWV of the solid from the same complex/ITO electrode re-dissolved in acetone after CPE (blue line, $c_{max}$ ~ 0.09 mM), and the same sample after addition 1 M of $H_2O$ (dashed red line); (**c**) and CV scans of the same solution as in (**b**), **inset**: scan rate dependence of the CV in the potential range of the detected $Fe^{3+/2+}$ redox couples. Cell setup for (**b**) and (**c**): BDD working el., non-aqueous $Ag^+/Ag$ ref. el., Pt counter-el., Ar atm., 25 °C, 0.1 M TBAP, SWV settings: $P_w$ = 80 ms ($f$ = 12.5 Hz), $P_H$ = 32 mV, $S_H$ = 4 mV.

As final comment, we note that upon solvation by water the [$Fe^{III}Cl_2$(tia-BAI)] complex might also rearrange to six-coordinate species, with one $Cl^-$ remaining in the coordination sphere beside the incoming aqua ligands. The five-coordinate [$Fe^{III}Cl(OH_2)$(tia-BAI)]$^{1+}$ could also prevail (Scheme 1), but the XPS and SEM-EDX results in combination with the electrochemical investigations on the re-dissolved samples after CPE do not support the presence of chloride. The lack of chloride from the used complex/ITO samples and the single $Fe^{3+/2+}$ redox peak in SWV (Figure 9b) identical to that resulting from the addition of water to acetone rather suggest [$Fe^{III}(H_2O)_2$(tia-BAI)]$^{2+}$ as the prevalent species responsible for prolonged water oxidation catalysis.

## 4. Conclusions

A heterocyclic pincer ligand was utilized in a $Fe^{III}$ dichloride complex (Figure 1), which served as precursor for the electrocatalyst aqua-form in water oxidation. Adjacent, labile sites were shown to favor $H_2O$ binding and WOC in the presence of 4N and NN′ ligands, but to our knowledge BAI NN′N pincer ligands have not been investigated so far. In this study we discussed the electrochemical properties of the [$Fe^{III}Cl_2$(tia-BAI)] complex in homogeneous water/acetone mixture to reveal the signatures of $Cl^-$ to $H_2O$ ligand exchange and proposed a molecular mechanism for the catalytic cycle. The redox activity of the pincer ligand seems to play a role in generating the proposed active form in WNA, [$Fe^{IV}$(O)($H_2O$)(tia-BAI$^{\bullet}$)]$^{2+}$ and it also possesses available sites for proton channeling in the course of further reaction steps. Importantly, the complex could be deposited to ITO as model anode from methanol that promotes ligand exchange of the precursor thus creating a catalytically active, solid ad-layer. In the case of this precursor type the selection of the solvent for drop-casting is of key importance to gain an active heterogenized WOC. The water-insolubility of the complex stems from the coordinated tia-BAI$^-$ ligand that seems to support surface attachment and leaves labile sites necessary for WOC, thus suitable for new molecular catalyst/(photo)anode hybrids. The route of catalyst deactivation appears to be demetalation of the complex, in which case the water-insoluble ancillary ligand still remains at the electrode that indicates its strong attachment to the surface. Similar pincer ligand containing complexes are in plan to influence the WOC activity of catalyst ad-layers and the chloride exchange properties of the complexes.

**Supplementary Materials:** The following are available online at http://www.mdpi.com/2624-781X/1/1/3/s1, Figure S1: SWVs of the tia-BAIH ligand and the [$Fe^{III}Cl_2$(tia-BAI)] complex in acetone, Figure S2: Comparison of CV scans for [$Fe^{III}Cl_2$(tia-BAI)] dissolved in acetone when 2 M of $H_2O$ or $D_2O$ is added, inset: CV scans of freshly prepared [$Fe^{III}Cl_2$(tia-BAI)] solutions used in the corresponding experiments and CVs recorded after the addition of $H_2O$ or $D_2O$, Table S1: Selected binding energy values from the fitting of XP spectra of a freshly drop-casted complex/ITO sample, and of those collected after 4.5 h of CPE at +1.4 V vs. Ag/AgCl in borate buffer at pH 8.3, Figure S3: (a) The S 2p and (b) the N 1 s binding energy region of XP spectra of the as-prepared complex/ITO with the fitted components; (c) and (d) the corresponding spectra after CPE.

**Author Contributions:** Conceptualization, J.S.P.; methodology, J.S.P., S.M.A.-Z., L.D., M.N. and K.F.; validation, T.B., S.M.A.-Z., D.L., M.N. and J.S.P.; investigation, S.M.A.-Z., D.L., T.B., K.F., M.N., L.I. and J.S.P.; resources, S.M.A.-Z. and J.S.P.; data curation, J.S.P.; writing—original draft preparation, S.M.A.-Z. and J.S.P.; writing—review and editing, S.M.A.-Z., D.L., T.B., K.F., M.N. and J.S.P.; visualization, S.M.A.-Z., M.N., D.L. and J.S.P.; supervision, J.S.P.; project administration, K.F. and J.S.P; funding acquisition, J.S.P. All authors have read and agreed to the published version of the manuscript.

**Funding:** This research is financed by the NKFI-128841 grant, and the VEKOP-2.3.2-16-2016-00011 grant supported by the European Structural and Investment Funds.

**Acknowledgments:** Technical help by Attila Kovács and Anna Szuja (technicians) is gratefully acknowledged.

**Conflicts of Interest:** The authors declare no conflict of interest. The funders had no role in the design of the study; in the collection, analyses, or interpretation of data; in the writing of the manuscript, or in the decision to publish the results.

## References


1. Dau, H.; Limberg, C.; Reier, T.; Risch, M.; Roggan, S.; Strasser, P. The mechanism of water oxidation: From electrolysis via homogeneous to biological catalysis. *ChemCatChem* **2010**, *2*, 724–761. [CrossRef]
2. Umena, Y.; Kawakami, K.; Shen, J.-R.; Kamiya, N. Crystal structure of oxygen-evolving photosystem II at a resolution of 1.9 Å. *Nature* **2011**, *473*, 55–60. [CrossRef] [PubMed]
3. Wu, L.; Eberhart, M.; Nayak, A.; Brennaman, M.K.; Shan, B.; Meyer, T.J. A molecular silane-derivatized Ru(II) catalyst for photoelectrochemical water oxidation. *J. Am. Chem. Soc.* **2018**, *140*, 15062–15069. [CrossRef] [PubMed]
4. Matheu, R.; Ertem, M.Z.; Gimbert-Suriñach, C.; Sala, X.; Llobet, A. Seven coordinated molecular ruthenium–water oxidation catalysts: A coordination chemistry journey. *Chem. Rev.* **2019**. [CrossRef] [PubMed]
5. Karlsson, E.A.; Lee, B.-L.; Åkermark, T.; Johnston, E.V.; Kärkäs, M.D.; Sun, J.; Hansson, Ö.; Bäckvall, J.-E.; Åkermark, B. Photosensitized water oxidation by use of a bioinspired manganese catalyst. *Angew. Chem. Int. Ed.* **2011**, *50*, 11715–11718. [CrossRef]
6. Kal, S.; Ayensu-Mensah, L.; Dinolfo, P.H. Evidence for catalytic water oxidation by a dimanganese tetrakis-Schiff base macrocycle. *Inorg. Chim. Acta* **2014**, *423*, 201–206. [CrossRef]
7. Dismukes, G.C.; Brimblecombe, R.; Felton, G.A.N.; Pryadun, R.S.; Sheats, J.E.; Spiccia, L.; Swiegers, G.F. Development of bioinspired $Mn_4O_4$—Cubane water oxidation catalysts: Lessons from photosynthesis. *Acc. Chem. Res.* **2009**, *42*, 1935–1943. [CrossRef]
8. Coggins, M.K.; Zhang, M.-T.; Vannucci, A.K.; Dares, C.J.; Meyer, T.J. Electrocatalytic water oxidation by a monomeric amidate-ligated Fe(III)—Aqua complex. *J. Am. Chem. Soc.* **2014**, *136*, 5531–5534. [CrossRef]
9. Okamura, M.; Kondo, M.; Kuga, R.; Kurashige, Y.; Yanai, T.; Hayami, S.; Praneeth, V.K.K.; Yoshida, M.; Yoneda, K.; Kawata, S.; et al. A pentanuclear iron catalyst designed for water oxidation. *Nature* **2016**, *530*, 465–468. [CrossRef]
10. Ellis, W.C.; McDaniel, N.D.; Bernhard, S.; Collins, T.J. Fast water oxidation using iron. *J. Am. Chem. Soc.* **2010**, *132*, 10990–10991. [CrossRef]
11. Al-Zuraiji, S.M.; Benkó, T.; Illés, L.; Németh, M.; Frey, K.; Sulyok, A.; Pap, J.S. Utilization of hydrophobic ligands for water-insoluble Fe(II) water oxidation catalysts—Immobilization and characterization. *J. Catal.* **2020**, *381*, 615–625. [CrossRef]
12. Younus, H.A.; Ahmad, N.; Chughtai, A.H.; Vandichel, M.; Busch, M.; Van Hecke, K.; Yusubov, M.; Song, S.; Verpoort, F. A robust molecular catalyst generated in situ for photo- and electrochemical water oxidation. *ChemSusChem* **2017**, *10*, 862–875. [CrossRef] [PubMed]
13. Chen, H.; Sun, Z.; Liu, X.; Han, A.; Du, P. Cobalt–salen complexes as catalyst precursors for electrocatalytic water oxidation at low overpotential. *J. Phys. Chem. C* **2015**, *119*, 8998–9004. [CrossRef]
14. Shevchenko, D.; Anderlund, M.F.; Thapper, A.; Styring, S. Photochemical water oxidation with visible light using a cobalt containing catalyst. *Energy Environ. Sci.* **2011**, *4*, 1284. [CrossRef]
15. Han, Y.; Wu, Y.; Lai, W.; Cao, R. Electrocatalytic water oxidation by a water-soluble nickel porphyrin complex at neutral pH with low overpotential. *Inorg. Chem.* **2015**, *54*, 5604–5613. [CrossRef]
16. Zhang, M.; Zhang, M.-T.; Hou, C.; Ke, Z.-F.; Lu, T.-B. Homogeneous electrocatalytic water oxidation at neutral ph by a robust macrocyclic nickel (II) complex. *Angew. Chem. Int. Ed.* **2014**, *53*, 13042–13048. [CrossRef]
17. Fisher, K.J.; Materna, K.L.; Mercado, B.Q.; Crabtree, R.H.; Brudvig, G.W. Electrocatalytic water oxidation by a copper(II) complex of an oxidation-resistant ligand. *ACS Catal.* **2017**, *7*, 3384–3387. [CrossRef]
18. Barnett, S.M.; Goldberg, K.I.; Mayer, J.M. A soluble copper–Bipyridine water-oxidation electrocatalyst. *Nat. Chem.* **2012**, *4*, 498–502. [CrossRef]
19. Chen, G.; Chen, L.; Ng, S.-M.; Man, W.-L.; Lau, T.-C. Chemical and visible-light-driven water oxidation by iron complexes at pH 7-9: Evidence for dual-active intermediates in iron-catalyzed water oxidation. *Angew. Chem. Int. Ed.* **2013**, *52*, 1789–1791. [CrossRef]
20. Casadevall, C.; Bucci, A.; Costas, M.; Lloret-Fillol, J. Water oxidation catalysis with well-defined molecular iron complexes. In *Advances in Inorganic Chemistry*; Elsevier: Amsterdam, The Netherlands, 2019; Volume 74, pp. 151–196, ISBN 978-0-12-816082-4.
21. McDonald, A.R.; Que, L. High-valent nonheme iron-oxo complexes: Synthesis, structure, and spectroscopy. *Coord. Chem. Rev.* **2013**, *257*, 414–428. [CrossRef]

22. Hohenberger, J.; Ray, K.; Meyer, K. The biology and chemistry of high-valent iron–oxo and iron–nitrido complexes. *Nat. Commun.* **2012**, *3*, 720. [CrossRef] [PubMed]
23. Huang, X.; Groves, J.T. Beyond ferryl-mediated hydroxylation: 40 years of the rebound mechanism and C–H activation. *JBIC J. Biol. Inorg. Chem.* **2017**, *22*, 185–207. [CrossRef] [PubMed]
24. Bauer, I.; Knölker, H.-J. Iron catalysis in organic synthesis. *Chem. Rev.* **2015**, *115*, 3170–3387. [CrossRef] [PubMed]
25. Fürstner, A. Iron catalysis in organic synthesis: A critical assessment of what it takes to make this base metal a multitasking champion. *ACS Cent. Sci.* **2016**, *2*, 778–789. [CrossRef]
26. Asraf, M.d.A.; Younus, H.A.; Yusubov, M.; Verpoort, F. Earth-abundant metal complexes as catalysts for water oxidation; is it homogeneous or heterogeneous? *Catal. Sci. Technol.* **2015**, *5*, 4901–4925. [CrossRef]
27. Codolà, Z.; Garcia-Bosch, I.; Acuña-Parés, F.; Prat, I.; Luis, J.M.; Costas, M.; Lloret-Fillol, J. Electronic effects on single-site iron catalysts for water oxidation. *Chem. Eur. J.* **2013**, *19*, 8042–8047. [CrossRef]
28. Elizarova, G.L.; Matvienko, L.G.; Lozhkina, N.V.; Maizlish, V.E.; Parmon, V.N. Homogeneous catalysts for dioxygen evolution from water. Oxidation of water by trisbipyridylruthenium (III) in the presence of metallophthalocyanines. *React. Kinet. Catal. Lett.* **1981**, *16*, 285–288. [CrossRef]
29. Abe, T.; Shiroishi, H.; Kinoshita, K.; Kaneko, M. Photoinduced water oxidation by polymeric iron cyanide complex. *Macromol. Symp.* **1998**, *131*, 81–86. [CrossRef]
30. Das, B.; Orthaber, A.; Ott, S.; Thapper, A. Iron pentapyridyl complexes as molecular water oxidation catalysts: Strong influence of a chloride ligand and pH in altering the mechanism. *ChemSusChem* **2016**, *9*, 1178–1186. [CrossRef]
31. Shylin, S.I.; Pavliuk, M.V.; D'Amario, L.; Mamedov, F.; Sá, J.; Berggren, G.; Fritsky, I.O. Efficient visible light-driven water oxidation catalysed by an iron(IV) clathrochelate complex. *Chem. Commun.* **2019**, *55*, 3335–3338. [CrossRef]
32. Shylin, S.I.; Pavliuk, M.V.; D'Amario, L.; Fritsky, I.O.; Berggren, G. Photoinduced hole transfer from tris(bipyridine)ruthenium dye to a high-valent iron-based water oxidation catalyst. *Faraday Discuss.* **2019**, *215*, 162–174. [CrossRef] [PubMed]
33. Das, B.; Thapper, A.; Ott, S.; Colbran, S.B. Structural features of molecular electrocatalysts in multi-electron redox processes for renewable energy-recent advances. *Sustain. Energy Fuels* **2019**, *3*, 2159–2175. [CrossRef]
34. Sinha, W.; Mahammed, A.; Fridman, N.; Gross, Z. Water oxidation catalysis by mono- and binuclear iron corroles. *ACS Catal.* **2020**, *10*, 3764–3772. [CrossRef]
35. Hong, Y.H.; Jung, J.; Nakagawa, T.; Sharma, N.; Lee, Y.-M.; Nam, W.; Fukuzumi, S. Photodriven oxidation of water by plastoquinone analogs with a nonheme iron catalyst. *J. Am. Chem. Soc.* **2019**, *141*, 6748–6754. [CrossRef]
36. Karim, S.; Chakraborty, A.; Samanta, D.; Zangrando, E.; Ghosh, T.; Das, D. A dinuclear iron complex as an efficient electrocatalyst for homogeneous water oxidation reaction. *Catal. Sci. Technol.* **2020**, *10*, 2830–2837. [CrossRef]
37. Praneeth, V.K.K.; Kondo, M.; Okamura, M.; Akai, T.; Izu, H.; Masaoka, S. Pentanuclear iron catalysts for water oxidation: Substituents provide two routes to control onset potentials. *Chem. Sci.* **2019**, *10*, 4628–4639. [CrossRef]
38. Panda, C.; Debgupta, J.; Díaz Díaz, D.; Singh, K.K.; Sen Gupta, S.; Dhar, B.B. Homogeneous photochemical water oxidation by biuret-modified fe-taml: Evidence of FeV(O) intermediate. *J. Am. Chem. Soc.* **2014**, *136*, 12273–12282. [CrossRef]
39. Codolà, Z.; Gamba, I.; Acuña-Parés, F.; Casadevall, C.; Clémancey, M.; Latour, J.-M.; Luis, J.M.; Lloret-Fillol, J.; Costas, M. Design of iron coordination complexes as highly active homogenous water oxidation catalysts by deuteration of oxidation-sensitive sites. *J. Am. Chem. Soc.* **2019**, *141*, 323–333. [CrossRef]
40. Lloret-Fillol, J.; Costas, M. Water oxidation at base metal molecular catalysts. In *Advances in Organometallic Chemistry*; Elsevier: Amsterdam, The Netherlands, 2019; Volume 71, pp. 1–52. ISBN 978-0-12-817115-8.
41. Zahran, Z.N.; Tsubonouchi, Y.; Mohamed, E.A.; Yagi, M. Recent advances in the development of molecular catalyst-based anodes for water oxidation toward artificial photosynthesis. *ChemSusChem* **2019**, *12*, 1775–1793. [CrossRef]
42. Wu, L.; Nayak, A.; Shao, J.; Meyer, T.J. Crossing the bridge from molecular catalysis to a heterogenous electrode in electrocatalytic water oxidation. *Proc. Natl. Acad. Sci. USA* **2019**, *116*, 11153–11158. [CrossRef]

43. Kottrup, K.G.; Hetterscheid, D.G.H. Evaluation of iron-based electrocatalysts for water oxidation-an on-line mass spectrometry approach. *Chem. Commun.* **2016**, *52*, 2643–2646. [CrossRef] [PubMed]
44. Kottrup, K.G.; D'Agostini, S.; van Langevelde, P.H.; Siegler, M.A.; Hetterscheid, D.G.H. Catalytic activity of an iron-based water oxidation catalyst: Substrate effects of graphitic electrodes. *ACS Catal.* **2018**, *8*, 1052–1061. [CrossRef] [PubMed]
45. Garrido-Barros, P.; Gimbert-Suriñach, C.; Moonshiram, D.; Picón, A.; Monge, P.; Batista, V.S.; Llobet, A. Electronic π-Delocalization boosts catalytic water oxidation by Cu(II) molecular catalysts heterogenized on graphene sheets. *J. Am. Chem. Soc.* **2017**, *139*, 12907–12910. [CrossRef] [PubMed]
46. Shi, T.; Li, H.; Ding, L.; You, F.; Ge, L.; Liu, Q.; Wang, K. Facile preparation of unsubstituted iron(II) phthalocyanine/carbon nitride nanocomposites: A multipurpose catalyst with reciprocally enhanced photo/electrocatalytic activity. *ACS Sustain. Chem. Eng.* **2019**, *7*, 3319–3328. [CrossRef]
47. Demeter, E.L.; Hilburg, S.L.; Washburn, N.R.; Collins, T.J.; Kitchin, J.R. Electrocatalytic oxygen evolution with an immobilized TAML activator. *J. Am. Chem. Soc.* **2014**, *136*, 5603–5606. [CrossRef]
48. Pap, J.S.; Draksharapu, A.; Giorgi, M.; Browne, W.R.; Kaizer, J.; Speier, G. Stabilisation of μ-peroxido-bridged Fe(III) intermediates with non-symmetric bidentate N-donor ligands. *Chem. Commun.* **2014**, *50*, 1326–1329. [CrossRef]
49. Lawrence, M.A.W.; Green, K.-A.; Nelson, P.N.; Lorraine, S.C. Review: Pincer ligands—Tunable, versatile and applicable. *Polyhedron* **2018**, *143*, 11–27. [CrossRef]
50. Csonka, R.; Speier, G.; Kaizer, J. Isoindoline-derived ligands and applications. *RSC Adv.* **2015**, *5*, 18401–18419. [CrossRef]
51. Váradi, T.; Pap, J.S.; Giorgi, M.; Párkányi, L.; Csay, T.; Speier, G.; Kaizer, J. Iron(III) complexes with meridional ligands as functional models of intradiol-cleaving catechol dioxygenases. *Inorg. Chem.* **2013**, *52*, 1559–1569. [CrossRef]
52. Kripli, B.; Baráth, G.; Balogh-Hergovich, É.; Giorgi, M.; Simaan, A.J.; Párkányi, L.; Pap, J.S.; Kaizer, J.; Speier, G. Correlation between the SOD-like activity of hexacoordinate iron(II) complexes and their $Fe^{3+}/Fe^{2+}$ redox potentials. *Inorg. Chem. Commun.* **2011**, *14*, 205–209. [CrossRef]
53. Pap, J.S.; Cranswick, M.A.; Balogh-Hergovich, É.; Baráth, G.; Giorgi, M.; Rohde, G.T.; Kaizer, J.; Speier, G.; Que, L. An Iron(II)[1,3-bis(2′-pyridylimino)isoindoline] complex as a catalyst for substrate oxidation with $H_2O$—Evidence for a transient peroxidodiiron(III) species. *Eur. J. Inorg. Chem.* **2013**, *2013*, 3858–3866. [CrossRef] [PubMed]
54. Scheja, A.; Baabe, D.; Menzel, D.; Pietzonka, C.; Schweyen, P.; Bröring, M. Spin crossover and valence tautomerism in neutral homoleptic iron complexes of Bis (pyridylimino) isoindolines. *Chem. Eur. J.* **2015**, *21*, 14196–14204. [CrossRef] [PubMed]
55. Semino, R.; Longinotti, M.P. Excess protons in water-acetone mixtures. II. A conductivity study. *J. Chem. Phys.* **2013**, *139*, 164510. [CrossRef] [PubMed]
56. Geary, W.J. The use of conductivity measurements in organic solvents for the characterisation of coordination compounds. *Coord. Chem. Rev.* **1971**, *7*, 81–122. [CrossRef]
57. Kruck, M.; Sauer, D.C.; Enders, M.; Wadepohl, H.; Gade, L.H. Bis(2-pyridylimino)isoindolato iron(ii) and cobalt(ii) complexes: Structural chemistry and paramagnetic NMR spectroscopy. *Dalton Trans.* **2011**, *40*, 10406. [CrossRef]
58. Acuña-Parés, F.; Codolà, Z.; Costas, M.; Luis, J.M.; Lloret-Fillol, J. Unraveling the mechanism of water oxidation catalyzed by nonheme iron complexes. *Chem. Eur. J.* **2014**, *20*, 5696–5707. [CrossRef]
59. Hoffert, W.A.; Mock, M.T.; Appel, A.M.; Yang, J.Y. Incorporation of hydrogen-bonding functionalities into the second coordination sphere of iron-based water-oxidation catalysts. *Eur. J. Inorg. Chem.* **2013**, *2013*, 3846–3857. [CrossRef]
60. Codolà, Z.; Gómez, L.; Kleespies, S.T.; Que, L., Jr.; Costas, M.; Lloret-Fillol, J. Evidence for an oxygen evolving iron–oxo–cerium intermediate in iron-catalysed water oxidation. *Nat. Commun.* **2015**, *6*, 5865. [CrossRef]
61. Ellingsworth, E.C.; Turner, B.; Szulczewski, G. Thermal conversion of $[Fe(phen)_3](SCN)_2$ thin films into the spin crossover complex $Fe(phen)_2(NCS)_2$. *RSC Adv.* **2013**, *3*, 3745. [CrossRef]
62. Li, L.; Craze, A.R.; Akiyoshi, R.; Tsukiashi, A.; Hayami, S.; Mustonen, O.; Bhadbhade, M.M.; Bhattacharyya, S.; Marjo, C.E.; Wang, Y.; et al. Direct monitoring of spin transitions in a dinuclear triple-stranded helicate iron(II) complex through X-ray photoelectron spectroscopy. *Dalton Trans.* **2018**, *47*, 2543–2548. [CrossRef]

63. Pronschinske, A.; Bruce, R.C.; Lewis, G.; Chen, Y.; Calzolari, A.; Buongiorno-Nardelli, M.; Shultz, D.A.; You, W.; Dougherty, D.B. Iron(ii) spin crossover films on Au(111): Scanning probe microscopy and photoelectron spectroscopy. *Chem. Commun.* **2013**, *49*, 10446. [CrossRef] [PubMed]
64. Floreano, L.; Cossaro, A.; Gotter, R.; Verdini, A.; Bavdek, G.; Evangelista, F.; Ruocco, A.; Morgante, A.; Cvetko, D. Periodic arrays of cu-phthalocyanine chains on Au(110). *J. Phys. Chem. C* **2008**, *112*, 10794–10802. [CrossRef]
65. Sarasola, A.; Abadía, M.; Rogero, C.; Garcia-Lekue, A. Theoretical insights into unexpected molecular core level shifts: Chemical and surface effects. *J. Phys. Chem. Lett.* **2017**, *8*, 5718–5724. [CrossRef] [PubMed]
66. Pap, J.S.; Bányai, V.; Szilvási, D.S.; Kaizer, J.; Speier, G.; Giorgi, M. Influence of meridional $N_3$-ligands on supramolecular assembling and redox behavior of carboxylatocopper(II) complexes. *Inorg. Chem. Commun.* **2011**, *14*, 1767–1772. [CrossRef]
67. Pap, J.S.; Kripli, B.; Bányai, V.; Giorgi, M.; Korecz, L.; Gajda, T.; Árus, D.; Kaizer, J.; Speier, G. Tetra-, penta- and hexacoordinate copper(II) complexes with $N_3$ donor isoindoline-based ligands: Characterization and SOD-like activity. *Inorg. Chim. Acta* **2011**, *376*, 158–169. [CrossRef]